

AEM
3

Distribution of Metal Cations in Ni-Mo-W Sulfide Catalysts

Jennifer Hein,^[a] Oliver Y. Gutiérrez,^{*[a]} Eva Schachtl,^[a] Pinghong Xu,^[b] Nigel D. Browning,^[c] Andreas Jentys,^[a] and Johannes A. Lercher^{*[a]}

The distribution of metal cations and the morphology of unsupported NiMo, NiW, and NiMoW sulfide catalysts were explored qualitatively and quantitatively. In the bi- and trimetallic catalysts, Mo(W)S₂ nanoparticles are deposited on Ni sulfide particles of varying stoichiometry and sizes (crystalline Ni₉S₈ and Ni₃S₄ were identified). These nanoparticles are stacks of Mo(W)S₂ slabs with varying size, degrees of bending and mismatch between the slabs. High resolution electron microscopy and X-ray absorption spectroscopy based on particle modeling

revealed a statistical distribution of Mo and W within individual layers in sulfide NiMoW, forming intralayer mixed Mo_{1-x}W_xS₂. Ni is associated with MoS₂, WS₂, and Mo_{1-x}W_xS₂ creating Ni-promoted phases. The incorporation of Ni at the edges of the slabs was the highest for sulfide NiMoW. This high concentration of Ni in sulfide NiMoW, as well as its long bent Mo_{1-x}W_xS₂ slabs, were paralleled by the highest activity for nitrogen and sulfur removal from model hydrocarbons such as *o*-propylaniline and dibenzothiophene.

Introduction

MoS₂ and WS₂ are isostructural and isomorphic semiconductors with a layered structure. The ability of MoS₂ and WS₂ to activate H₂ and to catalyze hydrogenation and hydrogenolysis of C–N and C–S bonds makes them interesting catalysts. Thus, MoS₂ and WS₂ (bulk and supported) have been widely applied as catalysts in hydrotreating of oil fractions,^[1–4] biomass-derived feedstocks,^[5] as well as in photo- and electrochemistry.^[6–8] The wide applicability triggered activities to synthesize well-defined morphologies and in turn tailored band structures.^[9,10] There has been also impressive progress in atom-level characterization of MoS₂ and WS₂.^[11,12] Most of these studies, however, focused on model catalysts, prepared under conditions facilitating the analysis (e.g., in situ monolayer growth). Wet chemistry prepared sulfide materials similar to those used industrially are significantly more complex and hardly accessible for these advanced characterizations. This holds also true for

the promotion of the MoS₂ and WS₂ by Ni²⁺ or Co²⁺ cations, which are mainly explored via averaging techniques such as XAS.^[13–15]

Although bimetallic catalysts are already challenging, trimetallic Ni-Mo-W sulfide materials make the task even more complex.^[16,17] Studies on the consequences of combining Mo and W in a single sulfide were in consequence only performed in the absence of Ni or Co.^[11,18,19]

The target of the current work is, therefore, to investigate the structure, morphology, and the distribution of catalyst constituents in three wet-chemically prepared sulfides qualitatively and quantitatively. We address not only the distribution of W and Mo, but also the location and nature of the incorporated Ni. A comprehensive EXAFS study of all three metal edges in combination with HAADF-STEM was used and combined with TEM, XRD, and Raman spectroscopy. Systematic comparison of theoretical EXAFS of model clusters was used to analyze in detail the influence of the backscatter Mo, W, and Ni at different distances. The impact of the physicochemical properties on catalytic activity was explored for nitrogen and sulfur removal from *o*-propylaniline and dibenzothiophene, respectively.

Experimental Section

Catalyst preparation: Two bimetallic, NiMoS and NiWS, and one trimetallic NiMoWS materials were prepared by a pH controlled coprecipitation in aqueous solution in accordance to Ref. [20]. The precursors were subsequently sulfided in 10 vol.% H₂S in H₂ flow at 400 °C and 1.8 MPa for 12 h. Ammonium heptamolybdate (AHM), ammonium metatungstate (AMT), Ni nitrate, aqueous ammonia and maleic acid were used as reactants during the synthesis.

Powder X-Ray diffraction (XRD): The crystal structure of the samples was determined by X-ray diffraction by using an X'Pert Pro

[a] J. Hein, Dr. O. Y. Gutiérrez, E. Schachtl, Prof. Dr. A. Jentys, Prof. Dr. J. A. Lercher
Department of Chemistry and Catalysis Research Center
Technische Universität München
Lichtenbergstraße 4, 85747 Garching (Germany)
Fax: (+49) 89-28913544
E-mail: oliver.gutierrez@mytum.de
johannes.lercher@ch.tum.de

[b] P. Xu
Department of Chemical Engineering and Materials Science
University of California-Davis
One Shields Avenue, Davis, CA 95616 (USA)

[c] Prof. Dr. N. D. Browning
Fundamental and Computational Sciences Directorate
Pacific Northwest National Laboratory
Richland, WA 99352 (USA)

Supporting Information for this article is available on the WWW under <http://dx.doi.org/10.1002/cctc.201500788>.

This publication is part of a Special Issue on "Microscopy and Spectroscopy for Catalysis". Once the full issue has been assembled, a link to its Table of Contents will appear here.

PW 3040/60 (PANalytical) diffractometer equipped with a copper X-ray tube, a Ni-K_β filter to obtain monochromatic Cu-K_{α1} radiation (0.154 nm) and a solid state detector (X'Celerator). The measurements were performed with a 10 × 10⁻⁹ m slit mask in a range from 2θ = 5° to 2θ = 70° at the operating conditions of 45 kV and 40 mA. The sulfided catalysts were measured for 1 h with step size of 0.017° and scan time of 115 s per step and for selected reference materials 5 min scans with a step size of 0.017° and 10 s per step were used. The crystallographic phases were identified by using the Inorganic Crystal Structure Database (ICSD).^[21] The Scherrer equation was used to determine the stacking degree of sulfide slabs in the catalysts, knowing that the diffraction at around 14° 2θ corresponds to the (002) plane with interplanar distance of 6.1 Å (distance between the metal cation layers in MoS₂ or WS₂). The measured full width at the half maximum (FWHM) was corrected by the diffractometer typical line broadening of 0.1 rad estimated by instrument calibration.

Raman Spectroscopy: Raman spectra were recorded with a Renishaw Raman system (Type 1000, dispersive spectrometer) equipped with CCD detector and a Leica microscope DM LM. The excitation wavelength of 514 nm was generated by a multi-line argon-ion gas laser (Stellar-Pro Select 150 of MODU-Laser) operating at 20 mW power. The wavenumber accuracy was within 1 cm⁻¹. Sulfide catalysts and reference materials were analyzed under ambient conditions in the form of self-supported wafers.

Electron microscopy: The morphology and particle size of the different samples were analyzed by electron microscopic methods. Standard measurements of the sulfide catalysts were performed in transmission mode coupled with selective area electron diffraction (TEM-SAED) with a JEM-2011 (JEOL) with an accelerating voltage of 120 keV. The average length of the sulfide slabs in the catalysts was estimated by the length measurements of around 500 different bundles of metal sulfide slabs from different sample spots. Moreover, high resolution scanning electron microscopy coupled with energy dispersive X-ray spectroscopy (HR-SEM-EDX) was performed with a high resolution FE-SEM, JSM 7500 F (JEOL) with EDX detector (Oxford). The HR-SEM micrographs were taken with the lower secondary electron imaging detector (LEI) and an accelerating voltage of 2 keV. Additionally, high-angle annular dark-field imaging with a scanning transmission electron microscope (HAADF-STEM) was performed using an aberration-corrected FEI Titan 80/300S. The device was operating at 80 keV and the HAADF collection inner angle was 75 mrad.

X-ray absorption spectroscopy (XAS): The structural properties of the sulfided catalysts were studied by X-ray absorption spectroscopy at the X1 beamline at HASYLAB, DESY, Hamburg, Germany. The data set was completed with experiments performed on the BM 26A-DUBBLE, (Dutch-Belgian) beamline at the ESRF, Grenoble, France. Spectra were recorded in transmission mode at the Mo K-edge (20000 eV), W L_{III}-edge (10207 eV) and at the Ni K-edge (8333 eV). Prior to EXAFS measurements, the sulfide catalysts were re-sulfided in the stainless steel in situ flow XAS cell.

Prior to the analysis of the experimental XAS data, a systematic EXAFS modeling was performed using mixed Mo_xW_yS₂ clusters created with Accelrys Material Studio 7.0 on the basis of the crystallographic structure of pure MoS₂ and WS₂. These mixed disulfide phases were used to calculate the Mo-W and W-Mo phase shifts and backscattering amplitudes at different distances using FEFF9 and VIPER.^[22,23] All XAS spectra were analyzed with the Demeter package (ATHENA and ARTEMIS, version 0.9.20) using FEFF6 and

IFEFFIT.^[24-25] After background removal and normalization to the average post-edge height to one, the oscillations were weighted with k^3 and Fourier-transformed within the limits of $k=2.5-14.0 \text{ \AA}^{-1}$. The local environments of the Mo, W, and Ni atoms in the sulfided catalysts were determined in k -space from the EXAFS. Single and multiple scattering phase shifts and backscattering amplitudes were calculated with FEFF^[25] based on crystallographic information files (cif files) of the ICSD^[21] and on the structure of model mixed Mo_xW_yS₂ clusters. The EXAFS at the Mo K-edge, W L_{III}-edge and at the Ni K-edge were simultaneously fitted. During fitting the Debye-Waller factor σ^2 and the distance r between two types of the metals were constrained to be equal (i.e. $r_{A-B}=r_{B-A}$) and the coordination numbers N_{A-B} and N_{B-A} were constrained by the molar ratio of A and B in the catalysts ($N_{A-B}/N_{B-A}=n(B)/n(A)$). The R factor and the absolute errors of all parameters, which are the estimated standard deviations and the statistical uncertainties of the starting parameter determined by IFEFFIT,^[24] were used to evaluate a certain fit result.

Catalytic activity studies: Kinetic studies were performed in a continuous flow trickle bed reactor system equipped with high pressure mass flow meters and a HPLC pump. The stainless steel, glass-coated tubular reactor was loaded with catalyst (0.025 g), diluted in SiC (1 g). The liquid samples were analyzed by off line gas chromatography (HP 6890 GC) equipped with a flame ionization detector and 60 m DB-17 capillary column. The hydrotreating reactions were performed as temperature dependent experiments at constant space-time of 49 h g_{cat} mol_{OPA}⁻¹ and total pressure of 5.0 MPa. Prior to the activity test reactions, the precursors were activated in situ in 10 vol.% H₂S in H₂ flow at 400 °C and 1.8 MPa for 12 h. The reactions were performed in excess of H₂ and with a mixture of hydrocarbons keeping the flow ratio of H₂ to liquid constant at 330 Ndm³dm⁻³. The initial reactant concentration was set to 1000 ppm N as *o*-propylaniline (OPA) in a mixture of 1000 ppm S as dimethyl disulfide (DMDS), 4.94 wt% hexadecane and 93.95 wt% tetradecane as solvent. Together with the OPA hydrodenitrogenation (HDN) activity, also the hydrodesulfurization (HDS) activity was studied by co-feeding 500 ppm S as dibenzothiophene (DBT) to the liquid feed. At the beginning of the experiment, a feed with OPA and DMDS was introduced at 370 °C. These starting conditions were kept for 48 h, although steady state conditions were usually reached after 24 h time on stream. Afterwards, the temperature was decreased to 360 and 350 °C and the liquid feed was changed to an OPA-DBT mixture to perform HDN and HDS simultaneously. After 30 h at 370 °C, the activity of the parallel HDN and HDS was also tested at 360 and 350 °C. At the end of the run, the initial reaction conditions (370 °C and pure OPA feed) were applied again. For all experiments, the same results were found after the initial stabilizing time of 48 h and at the end of the run.

Results and discussion

Composition and crystallinity

The composition of NiMoS, NiWS and the trimetallic NiMoWS sulfide are summarized in Table 1. All materials had similar Ni molar fractions and the molar ratio of Mo to W in the trimetallic catalyst was 1.3.

The XRD patterns showed Mo(W)S₂ and Ni sulfide phases as well as an X-ray amorphous material in all catalysts (Figure 1). The reference materials, MoS₂, WS₂, and Ni₃S₂ are shown for comparison. The reflections of all references are in agreement

Catalyst	Composition [mmol g ⁻¹]			X_{Ni} [mol/mol]	Av. stacking degree of MoS ₂ and WS ₂ ^[a]
	Ni	Mo	W		
NiMoS	4.6	3.7		0.55	5.7
NiMoWS	4.0	1.8	1.4	0.56	5.1
NiWS	2.5		2.8	0.47	4.4

[a] Average number of slabs forming a MoS₂ particle as determined by applying the Scherrer-equation on the (002) reflection at 14.2° 2θ which, is associated to the interplanar distance of 6.1 Å.

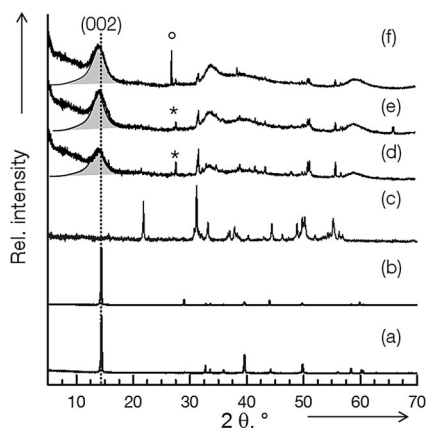


Figure 1. XRD pattern of the reference bulk materials a) MoS₂, b) WS₂, and c) Ni₃S₂, and of the unsupported sulfide catalysts d) NiMoS, e) NiMoWS, and f) NiWS. The profiles fitted under the (002) reflection at around 14.2° 2θ (grey filled) were used to determine the stacking degree of the MoS₂ and WS₂ slabs. The most important reflection of Ni₉S₈ (*) and Ni₃S₄ (°) are indicated.

with the data published in the ICSD database (#MoS₂: 644245; #WS₂: 202366; #Ni₃S₂: 27521).^[21] Sharp signals in the patterns of the sulfide catalysts correspond to different Ni sulfides. In NiMoS and NiMoWS, orthorhombic Ni₉S₈ (ICSD#: 63080) was the dominant phase (as indicated by the intense reflection at 27.4° 2θ) with traces of trigonal Ni₃S₂ (21.9° 2θ). The reflection at 26.6° 2θ in NiWS is assigned to the cubic phase of Ni₃S₄ (ICSD#: 57435). Additionally, Ni₉S₈ was found in low amounts in NiWS.

Broad reflections at 14.2, 33, 40 and 60° 2θ are assigned to hexagonal phases of MoS₂ and WS₂. The (002) reflection around 14.2° 2θ of the catalysts appeared at smaller angles compared to the references. In NiWS this reflection was observed at 14.0° 2θ, for NiMoWS at 14.1° 2θ, and for NiMoS at 14.2° 2θ. This indicates that the lattice parameters *d* (i.e., the distance between the metal sulfide layers) for the catalysts are between 6.32 and 6.23 Å, whereas the distance between the stacked layers in the bulk reference materials is 6.15 Å in WS₂ (14.4° 2θ) and 6.1 Å in MoS₂ (14.5° 2θ). This difference reflects disorder of the metal sulfide layers, e.g., bending, which occurs when the slabs grow significantly longer in the *x* and *y* direction than in the *z* direction.^[16] Additionally, line broadening and the amorphous background, especially at low diffraction

angles, are an indication for turbostratic disorder and uncorrelated single sulfide layers.^[26,27]

Raman spectroscopic characterization

Raman spectra of catalysts and reference materials are shown in Figure 2. The assignment of the bands is described in the

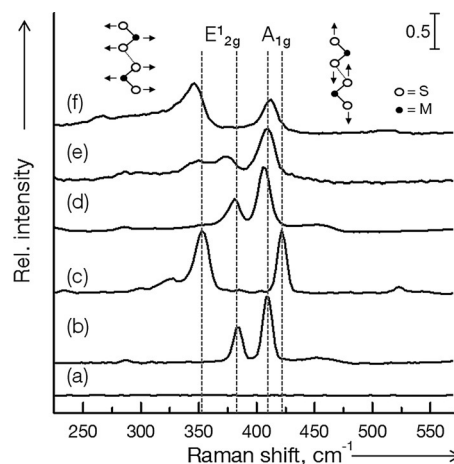


Figure 2. Raman spectra ($\lambda_{\text{exc}} = 514 \text{ nm}$) of the reference Ni₃S₂ (a; no Raman bands), b) MoS₂, and c) WS₂, and of the unsupported sulfided catalysts d) NiMoS, e) NiMoWS, and f) NiWS. The shift of the most intense Raman bands of the references are indicated by the dotted vertical lines and the corresponding atomic displacement of the E¹_{2g} (left) and A¹_g (right) mode is illustrated.

Supporting Information. Direct evidence for Ni sulfides was not obtained through Raman spectroscopy.

In the sulfide catalysts NiMoS and NiWS, only the A_{1g} and E¹_{2g} modes were observed (Figure 2(d) and (f)). The corresponding bands were shifted to lower wavenumbers and were broader than the bands of the reference materials. For instance, the A_{1g} mode appeared at 405 cm⁻¹ for NiMoS, and at 413 cm⁻¹ for NiWS (in the reference materials this band appeared at 409 cm⁻¹ for MoS₂ and 421 cm⁻¹ for WS₂). The downward shift was attributed to weaker metal sulfur bonds caused by the low stacking degree in the catalysts and the concomitant weak van der Waals forces, which allow atom displacement.^[28] The asymmetry of the bands of A_{1g} and E¹_{2g} modes was concluded to be caused by highly bent slabs, which influenced the symmetry selection rules leading to a second-order Raman signal, which overlapped with A_{1g} and E¹_{2g} bands.^[29]

The spectrum of NiMoWS (Figure 2(e)) appears to be a combination of the spectra of the bimetallic catalysts. The band at 410 cm⁻¹ is assigned to the A_{1g} mode of Mo-W composite species.^[30] The bands at 374 cm⁻¹ and 349 cm⁻¹ are assigned to E¹_{2g} modes of Mo-S and W-S, respectively, in agreement with observations when W systematically replaced Mo in Mo(W)S₂ crystals.^[19] The shift of both E¹_{2g} modes, compared to the references MoS₂ and WS₂, is attributed to a structural disorder of the sulfide slabs.

Electron microscopic characterization

Figure 3(C) shows a representative HR-SEM image of NiMoWS. The microstructure of the catalysts consists of large Ni_xS_y crystals (only Ni and S in a ratio of 1:1 are observed by EDX mapping) covered by spherical particles identified as MoS_2 or WS_2 by EDX mapping. Interestingly, Ni and S were identified across the whole sample, whereas Mo and W were detected only in the round pellets. The characterization by scanning He ion microscopy (SHIM) of all catalysts confirms the observations made by HR-SEM (Supporting Information).

Micrographs obtained by TEM (Figure 3A for NiMoWS and S1 of the supporting information) show that the sulfide agglomerates contained crystalline domains with varying sizes in the order of nanometers. The averaged stacking degree of around five for NiMoWS in the small crystals is in good agree-

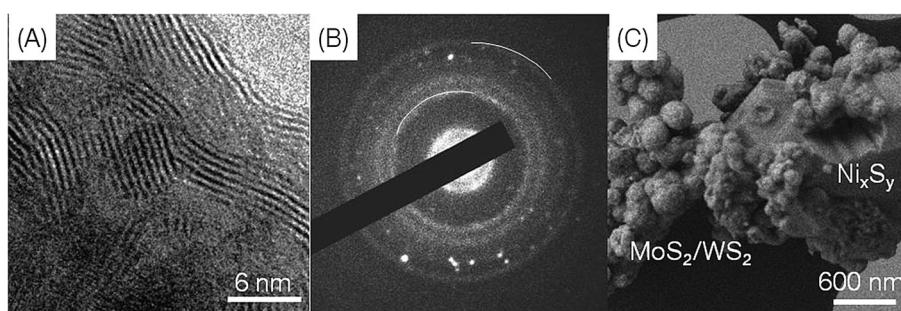


Figure 3. Representative electron microscopy images study of sulfide NiMoWS; a) TEM image, B) selective area electron diffraction, and C) HR-SEM image. The rings in (B) and stacked pellets in (C) are identified as MoS_2 and WS_2 phases, whereas the dots in (B) and the large particles in (C) belong to different Ni sulfides.

ment with the values obtained from XRD (Table 1). Furthermore, the structural disorder, i.e., bending (the MoS_2 slabs are not straight along the x and y axis), and random orientation of the crystal domains observed in the micrographs is consistent with the increased lattice parameters in z direction derived from XRD and the shifts and asymmetry of the Raman signals of the A_{1g} and E_{2g}^1 modes. The longest slabs were found for NiMoWS with an average length of 20 nm, whereas slabs of 15 nm and 10 nm were present in NiWS and NiMoS, respectively. The presence of Ni_xS_y species associated to WS_2 and MoS_2 was confirmed by electron diffraction (SAED) of selected area. For instance, Figure 3(B) shows the SAED of NiMoWS, where the dots corresponded to single Ni_9S_8 crystals (interplanar distances of 2.8, 2.6, 2.3, 1.8, and 1.7 Å according to ICSD#: 63080^[21]). The presence of MoS_2/WS_2 phases was indicated by the broad rings in agreement with the broad reflections in the XRD patterns.

Hence, all catalysts are concluded to contain mixtures of sulfide phases. MoS_2 or WS_2 slabs form stacks with a relatively high degree of disorder, i.e., bending and misalignment among them. In turn, these microcrystalline domains agglomerate with random orientations forming spherical particles. Nickel sulfides exist in a variety of phases and particle sizes ranging from very large (few microns), which act as support for Mo(W)S_2 agglomerates and may produce diffraction pat-

terns (Figure 3(B)), to small particles, which seem to be occluded inside the Mo(W)S_2 agglomerates.

Aberration corrected HAADF-STEM with atomic resolution was used to analyze the sulfide slabs with their basal (001) plane parallel and perpendicular to the electron beam (Figure 4). Figure 5(A) shows a representative HAADF-STEM image of the top view of the basal plane of NiMoWS. The fact that particles do not exhibit sharp edge structures is attributed to the non-aligned terminations of the stacked sulfide slabs.^[31]

The distance between the bright spots assigned to Mo or W atoms is around 0.6 nm, which matches the distance of the second metal–metal coordination sphere of the hexagonal lattice of metal disulfides (5.48 Å). Additionally, the ADF profile shows weak signals in a distance of 0.2 nm from W and Mo, which are assigned to S atoms.^[11,31] The appearance of relatively bright and dark spots with different contrast (within 3 Å)

next to each other in Mo or W positions hints to the presence of projections of metal atoms with very different averaged molar mass in the same sulfide slab. We propose that this corresponds to the preferred presence of Mo and W forming bimetallic sulfide slabs, as also indicated by Raman spectroscopy. Such differences in Z -contrast were also used to deduce the formation of mixed $\text{Mo}_{1-x}\text{W}_x\text{S}_2$ layers by ADF studies of model $\text{Mo}_{1-x}\text{W}_x\text{S}_2$ particles combined

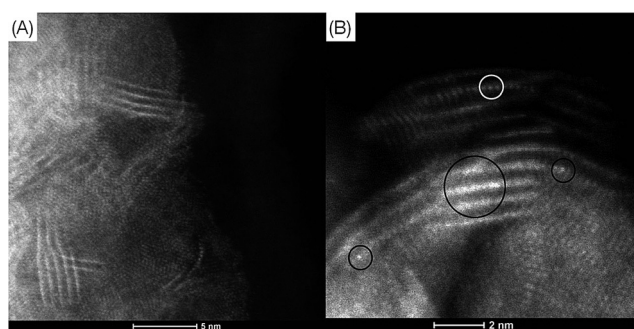


Figure 4. Aberration-corrected HAADF-STEM image of the sulfided NiMoWS catalyst; A) overview image at 300 keV, B) side view in [001] direction at 80 keV. The brighter atoms indicate the heaviest element in NiMoWS, that is, W atoms (marked by the circles).

with atomically resolved electron energy loss spectroscopy (EELS).^[11]

In contrast to microscopy studies of monolayers or cleaved single crystals reported,^[9,12,31] strong Z -contrast of atoms and perfectly resolved ADF images are not expected for the multi-layer bent structures studied. On the other hand, Ni atoms, if incorporated to the Mo(W)S_2 structure should be located at the edges of the slabs, according to the Co(Ni)–Mo–S model.

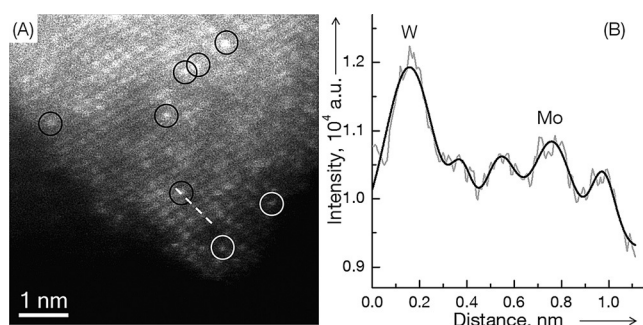


Figure 5. Representative aberration-corrected HAADF STEM image at 80 kV of the sulfided NiMoWS catalyst; A) top view, MS_2 [001] direction along the electron beam, B) distribution of the ADF counts along the indicated white line in (A). The circles indicate the heavier and therefore brighter W atoms.

However, identification of a third element by differences in Z-contrast was not possible due to the less defined edges of the slabs and the qualitative nature of the HAADF-STEM image analysis. In order to unequivocally establish the formation of mixed Mo-W sulfides within one layer level and to elucidate the interaction of Mo(W) S_2 with Ni, detailed analysis of the X-ray absorption spectra is required.

X-ray absorption spectroscopy

The formation of intralayer $Mo_{1-x}W_xS_2$ slabs in NiMoWS has to be reflected by Mo-W and W-Mo contributions at 3.16 Å, whereas the scattering between Ni and the other metals should be observed in higher coordination spheres. The X-ray absorption near edge structure (XANES) at the Ni and Mo K-edge as well as at the W L_{III} -edge are summarized in the Supporting Information (Figure S3). The corresponding Fourier transforms (FT) of the k^3 weighted extended X-ray absorption fine structure (EXAFS) are presented in Figure 6. Detailed descriptions of the XANES and of the corresponding linear combination fittings are presented in the Supporting Information.

The first contributions in the Fourier transforms of the EXAFS at the Ni K-edge of the catalysts (Figure 6(A)), at around 2 Å (not phase-shift corrected) is assigned to Ni-S^[14] contributions, which shifted to lower distances compared to Ni₃S₂. A

second pronounced contribution at around 3.5 Å (not phase-shift corrected) was assigned to Ni-Ni contributions in Ni₃S₂ (ICSD #27521^[21]). In the catalysts, this contribution is very weak. The FT of the EXAFS at the Mo K-edge and at the W L_{III} -edge are shown in Figure 6(B) and (C), respectively. The contributions of Mo-S^[14] and W-S^[32] were observed around 2 Å (not phase-shift corrected). The same distances (and similar intensities at the Mo K-edge) were found for the references and the catalysts. The second shell contributions at around 3 Å (not phase-shift corrected) at both edges were assigned to metal backscatter within the Mo(W) S_2 structure.^[14,32] At both edges (Mo K, and W L_{III}), the metal-metal contributions were weaker in the catalysts than in the references. In NiMoWS the intensities of the second shell contributions were even lower than the FT-EXAFS of the bimetallic one.

The weak metal-metal contributions at around 3 Å in NiMoWS might be explained by the rather poor alignment of the atoms in the short and bent MoS₂ or WS₂ slabs.^[32,33] However, this apparently contradicts the conclusions from XRD, Raman spectroscopy, and electron microscopy that the slabs in NiMoWS are ordered and are the largest among the studied materials. The reason for the weak metal-metal contributions in the FT is attributed to the specifics of the k^3 weighted EXAFS of the catalysts at the Mo K-edge and W L_{III} -edge and the corresponding bulk reference materials in Figure 7 (the k^3 weighted EXAFS functions of the samples at the Ni K-edge are presented in Figure S7 of the Supporting Information). Note that the amplitudes of the oscillations were weaker for the catalysts and the fine structure was less pronounced. Moreover, at the Mo K-edge and the W L_{III} -edge, the EXAFS of the trimetallic NiMoWS catalyst was different from the reference and the bimetallic catalysts between 9 and 16 Å⁻¹. These differences in the EXAFS could be caused by neighboring atoms with opposite backscattering phases like Mo and W,^[34,35] resulting in destructive interference. This is in line with the intralayer $Mo_{1-x}W_xS_2$ mixed sulfides suggested by HAADF-STEM.^[31,32] To assign the amplitudes and phase shifts of the M-M absorber-backscatter pairs, a series of mixed $Mo_{1-x}W_xS_2$ model clusters was generated based on the structure of MS_2 and the corresponding EXAFS were calculated. Special emphasis was given to the different backscattering of Mo and W atoms at the Mo

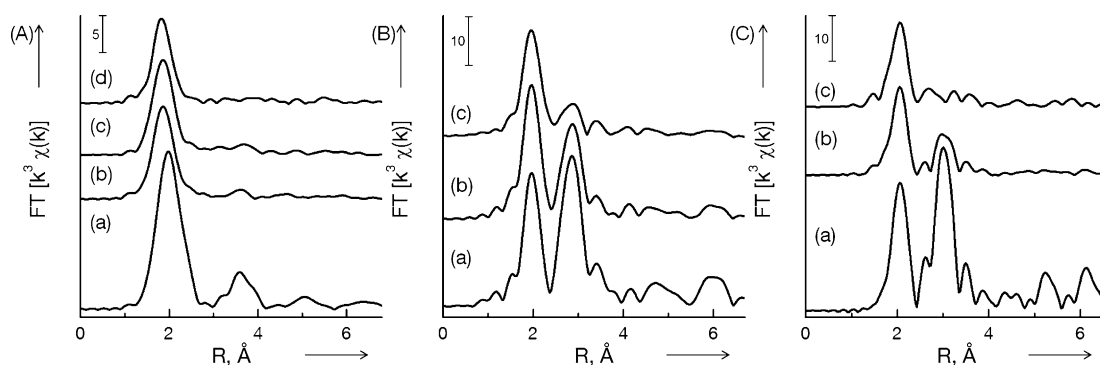


Figure 6. Fourier transforms of k^3 weighted EXAFS at the A) Ni K-edge, B) Mo K-edge, and C) W L_{III} -edge of the references; Ni₃S₂ (A,a), MoS₂ (B,a), and WS₂ (C,a), as well as of the catalysts NiMoS (A,b and B,b), NiMoWS (c), and NiWS (A,d and C,b).

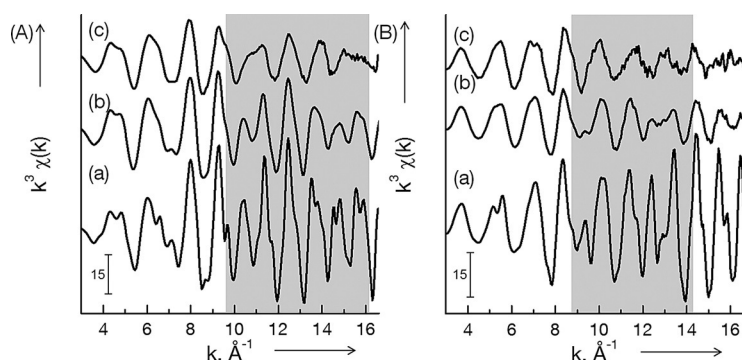


Figure 7. EXAFS at the A) Mo K-edge and at the B) W L_{III} -edge of MoS_2 (A, a), WS_2 (B, a) and of the catalysts NiMoS (A, b), NiWS (B, b), and NiMoWS (c). In the grey highlighted region, the EXAFS differ strongly from each other.

K- and at the W L_{III} -edges, respectively. Intralayer and interlayer mixtures were included as model clusters as well as different intermetallic arrangements and coordination numbers.

EXAFS of interlayer and intralayer mixed $\text{Mo}_{1-x}\text{W}_x\text{S}_2$ model particles

A MoS_2 particle ($16 \times 16 \text{ \AA}$) was created by using 5 hexagonal unit cells in a - and b -direction, which corresponds to two stacked sulfide layers containing 5 Mo atoms in a and b -direction (presented in the Supporting Information as Particle 1). The EXAFS function and its Fourier transformation are presented in Figure S8. The oscillations of the Mo-S scattering dominate in the lower k region up to 8 \AA^{-1} , whereas the metallic backscatter (i.e., the element with the higher molecule weight) determines the backscattering in the higher k region. As predicted by the EXAFS function,^[36] the most intense oscillations were found for the two next neighbors at $r_{\text{Mo-S}} = 2.41 \text{ \AA}$ and $r_{\text{Mo-Mo}} = 3.16 \text{ \AA}$. However, the backscattering of the more distant neighbors is needed to describe the structure as visualized by Figure S8(C) and (D). Note that the approach using the crystallographic structure describes perfectly ordered, and large particles (where most of the atoms have full coordination) leading to the highest possible intensity of the oscillations. The coordination number of the next neighbors and at a distance of 6.42 \AA , i.e., $N_{\text{Mo-S}}$ and $N_{\text{Mo-Mo}}$ is, therefore, 6 for the model Particle 1 (also $N_{\text{Mo-Mo}}$ is 6 at a distance of 6.42 \AA).

In distorted particles, the structural disorder leads to a decrease in the intensity of the oscillations at higher k values, which are typically accounted for in the analysis of the EXAFS by including higher Debye-Waller terms. However, the metal-metal coordination number is reduced for MoS_2 particles with high distortion and disorder, especially at the particle edges.^[33] Bending or distortion, as observed for the investigated sulfides, causes also differences in the bond distances of the metal-metal neighbors for a few atoms such as in edge distorted particles. Therefore, bending

could reduce the coordination number at the specific distance. This is the focus of an ongoing theoretical EXAFS investigation. For the present case, it suffices to understand the intermetallic interactions using the small 5×5 particles with two layers and the central metal atoms as absorber.

Let us analyze next the incorporation of W into the MoS_2 lattice. For the first possibility of model clusters, interlayer mixed $\text{Mo}_{1-x}\text{W}_x\text{S}_2$ particles, Mo and W disulfide layers were stacked in different sequences to reach a stacking degree of 6 (similar to that found by TEM and XRD for NiMoWS). The chosen stacking sequences were *abbaab* and *ababab*, where a stands for the $[\text{MoS}_2]$ layer and b for the $[\text{WS}_2]$ layer. The Mo-W coordination number at 6.42 \AA was varied from 0 for a monometallic disulfide slab over 3 for the *abbaab* stacking sequence to the maximum number possible of 6 in the *ababab* sequence. Additionally, clusters of different sizes and shapes were created.

Selected clusters are presented in the Supporting Information as Particle 2, and the corresponding EXAFS and FT at the Mo K-edge are shown in Figure 8. In comparison to the pure MoS_2 cluster, the Mo EXAFS has new weak features at 12.5 and 15 \AA^{-1} , especially for $N_{\text{Mo-W}} = 6$ (Figure 8(A, c)). However, the presence of W in the next sulfide layers is just slightly noticeable in the Mo EXAFS and FT. Increasing size or a hexagonal shape for the sulfide layer does not change the EXAFS oscillations. These observations demonstrate that the distance to the next layer at 6.42 \AA is too far away to influence the EXAFS of the absorber Mo atom significantly.

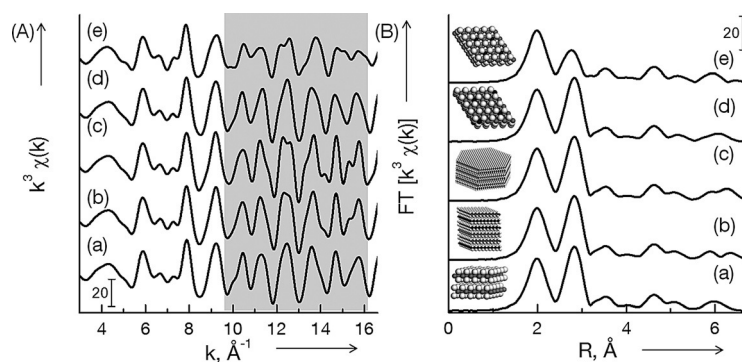


Figure 8. EXAFS at the Mo K-edge and the corresponding Fourier transforms of MoS_2 (a), MoWS_2 with Mo-W = 3 at 6.42 \AA , stacking sequence *abbaab* (b), MoWS_2 with Mo-W = 6 at 6.42 \AA , stacking sequence *ababab* (c), MoWS_2 with Mo-W = 2 at 5.48 \AA (d), MoWS_2 with Mo-W = 2 at 3.16 \AA (e). The used particles are also shown in Supporting Information (Color code: grey = Mo, black = W, light grey = S).

On the other hand, the particle size or shape does not influence the calculated phase shifts and amplitudes for the central Mo atom, whereas the coordination number averaged over the whole particle is influenced by size and particle shape. The squared MoS_2 particle with 5×5 Mo atoms (Particle 1) has average $N_{\text{Mo-S}} = 5.2$ and $N_{\text{Mo-Mo}} = 4.5$. These values increase with particle size and change with the shape. For the 9×9 *abbaab*

MoWS₂ particle (Particle 2(b)) the coordination numbers were $N_{\text{Mo-S}} = N_{\text{W-S}} = 5.6$ and $N_{\text{Mo-Mo}} = N_{\text{W-W}} = 5.1$, whereas for the hexagonal *ababab* MoWS₂ particle with a diagonal of 27 Mo atoms (a good representation of the investigated catalysts) $N_{\text{Mo-S}} = N_{\text{W-S}} = 5.9$ and $N_{\text{Mo-Mo}} = N_{\text{W-W}} = 5.7$ were calculated (Particle 2(c)).

To determine the influence of Mo-W interactions on the EXAFS of model clusters with Mo and W in the same slabs, W atoms were incorporated within a layer of MoS₂ (Particle 2(d) and (e) in the Supporting Information). These clusters contain 4 W atoms and 21 Mo atoms per sulfide layer and mixed metallic coordination numbers of 2. In Particle 2(d), two Mo atoms were replaced by W at 6.33 Å and 5.48 Å with regard to the central Mo atom. In Particle 2(e), a coordination number of $N_{\text{Mo-W}} = 2$ was calculated at distances of $r_{\text{Mo-W}} = 5.48$ Å and 3.16 Å. The EXAFS and the corresponding FT calculated for these particles are shown in Figure 8. The EXAFS of the Particle 2(d) with long Mo-W distances were very similar to those of pure MoS₂, i.e., the coordination number of $N_{\text{Mo-W}} = 2$ is too low and the distance between Mo and W atoms is too large to influence the overall EXAFS. Interestingly, the presence of W at $r_{\text{Mo-W}} = 3.16$ Å in Particle 2(e) has a large influence on the EXAFS despite the low coordination number of $N_{\text{Mo-W}} = 2$. The EXAFS oscillations change between $k = 10$ – 16 Å⁻¹ and the second contribution in the FT at around 3 Å is strongly reduced compared to pure MoS₂, similar to the EXAFS observed for the unsupported NiMoWS sulfide catalyst.

The analysis of the EXAFS of model clusters demonstrates that the formation of structures containing MoS₂ next to WS₂ phases cannot be ruled out by XAS. On the other hand, the theoretical EXAFS shows that the presence of the intralayer mixed Mo_{1-x}W_xS₂ EXAFS of NiMoWS is clearly established.

After concluding that Mo and W form intralayer MoWS₂ mixtures in NiMoWS, several intralayer Mo_{1-x}W_xS₂ clusters consisting of two layers with 5 × 5 atoms and varying $N_{\text{Mo-W}}$ at $r_{\text{Mo-W}} = 3.16$ Å were created and the corresponding EXAFS were calculated (Particles 2(d) and 2(e) were already discussed). Other clusters in this series with Mo and W as central atom are presented as Particle 3 and Particle 4 in the Supporting Information. Clusters with $N_{\text{Mo-W}}$ of 0, 1, 2, 3, 4, and 6 were generated by this approach. As the first metal–sulfur contribution at 2.4 Å was not influenced by the replacement of Mo by W (see Figure 8) only metal–metal scattering paths of the model clusters are discussed in the following.

The EXAFS of an absorber-backscatter pair is the result of the interference between the outgoing spherical wave of the photoelectron generated by the absorption process and the spherical wave backscattered from the neighboring atoms. The phase differences of both waves depend on the type of the atoms involved and distance between them. As an example, the phase functions (shown in the Supporting Information) were calculated at $k = 11.34$ Å⁻¹ as $\phi_{\text{Mo-Mo}} = 1.42\pi$, $\phi_{\text{Mo-W}} = 2.41\pi$ at the Mo K-edge, and $\phi_{\text{W-W}} = 4.38\pi$, and $\phi_{\text{W-Mo}} = 3.39\pi$ at the W L_{III}-edge by using tabulated phase shifts.^[37] These values indicate that the phase functions of these particular absorber-backscatter pairs are shifted by π at both metal edges. Subsequently, the EXAFS of the metal–metal scattering paths

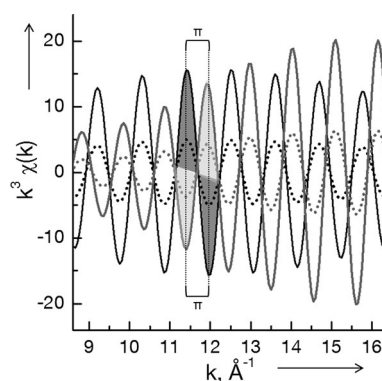


Figure 9. Calculated k^3 weighted Mo-Mo paths (black lines) and Mo-W paths (grey lines) at 3.16 Å at the Mo K-edge visualize the π shift between both scattering paths (solid lines correspond to $N(\text{M-M}) = 6$ and dotted lines to $N(\text{M-M}) = 2$).

were calculated with different coordination numbers (Figure 9). The π shift between the two scattering paths was observed in a wide range between 9 and 14 Å⁻¹ and was consistent for different coordination numbers and distances. The presence of both scattering paths in one sample leads to a destructive interference. Therefore, the EXAFS of an Mo/W = 1:1 solid solution in a Mo_{1-x}W_xS₂ system with a homogeneous dispersion of Mo and W is only determined by the metal–sulfur atom-backscatter pairs in the k range from 9 to 14 Å⁻¹.

Figure S9 shows all involved single scattering paths and the resulting overall EXAFS and FT of the 5 × 5 mixed sulfide cluster with $N_{\text{Mo-W}} = 3$ at $r_{\text{Mo-W}} = 3.16$ Å (Particle 3(f)) at the Mo K-edge. The metal–sulfur paths are dominant, although complete extinction of the metal–metal contributions does not occur. All EXAFS and the corresponding FT for the clusters created (Particles 3 and 4) are presented in Figure S10 for the Mo K-edge and in Figure S11 for the W L_{III}-edge. The EXAFS oscillations and their FT at both edges strongly changed in the region $k = 9$ – 16 Å⁻¹ for clusters with varying intermetallic coordination number at $r = 3.16$ Å. The second metal–metal contribution steadily decreases with increasing mixed metallic coordination number starting from a value for $N_{\text{Mo-W}}$ and $N_{\text{W-Mo}}$ of 2. Furthermore, a splitting of the signal was observed and the lowest intensity was obtained for $N_{\text{Mo-W}} = 3$ and $N_{\text{W-Mo}} = 2$.

The experimental data of NiMoWS catalyst and the EXAFS of model clusters are compared at the Mo K-edge and the W L_{III}-edge in Figures 10 and 11. For the experimental data, the intensity was lower and less features are visible in the EXAFS as well as in FT compared to the model clusters. This indicates that the NiMoWS catalyst does not have a long-range crystalline structure and consists of different phases.

Figures 10 and 11 also allow a qualitative comparison of the EXAFS of NiMoWS with those of the model clusters, the patterns of NiMoWS (shown in the lines labelled with (d)) fit well between the model patterns with $N = 2$ and $N = 3$. Therefore, mixed metallic coordination numbers between 2 and 3 exist in NiMoWS. Thus, for the final EXAFS fitting (multi-edge fitting), the theoretical FEFF-paths of the clusters with $N(\text{Mo-W})$ and $N(\text{W-Mo})$ of 3 and 2, respectively, were used.

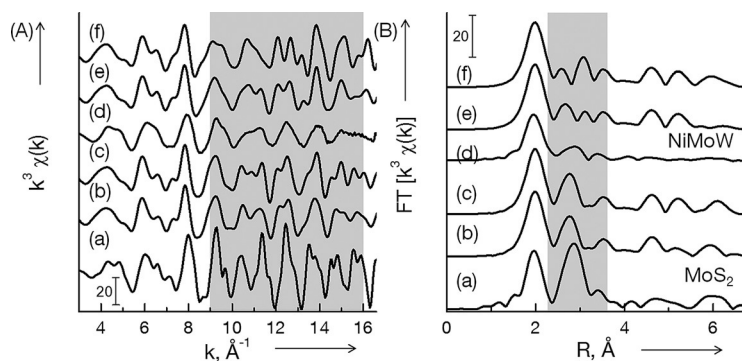


Figure 10. Experimental EXAFS of NiMoWS compared to EXAFS at the Mo K-edge (A) and the corresponding Fourier transforms (B) of model MoWS₂ with varying Mo-W coordination number N at 3.16 Å, namely MoS₂ bulk reference (a), MoWS₂ with $N_{\text{Mo-W}}=2$ and $N_{\text{W-Mo}}=6$ (b), MoWS₂ with $N_{\text{Mo-W}}=2$ and $N_{\text{W-Mo}}=2$ (c), NiMoWS catalyst (d), MoWS₂ with $N=3$ (e), and MoWS₂ with $N=4$ (f).

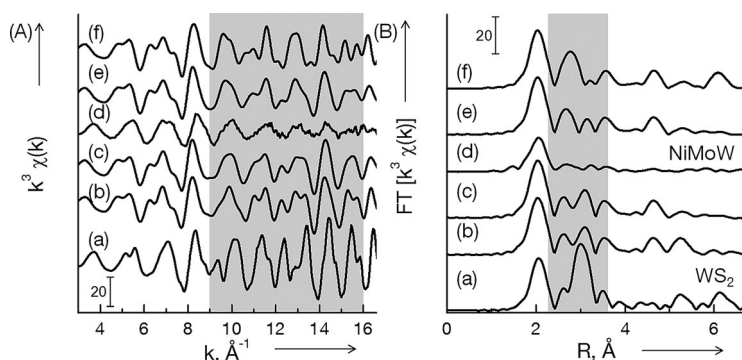


Figure 11. Experimental EXAFS of NiMoWS compared to the EXAFS at the W L_{III}-edge (A) and the corresponding Fourier transforms (B) of model MoWS₂ clusters with varying W-Mo coordination number N at 3.16 Å, namely WS₂ bulk reference (a), MoWS₂ with $N_{\text{W-Mo}}=2$ and $N_{\text{Mo-W}}=6$ (b), MoWS₂ with $N_{\text{W-Mo}}=2$ and $N_{\text{Mo-W}}=2$ (c), NiMoWS catalyst (d), MoWS₂ with $N=3$ (e), and MoWS₂ with $N=4$ (f).

EXAFS analysis

In the discussion above, we have demonstrated that the X-ray absorption spectra suggest the presence of intralayer Mo_{1-x}W_xS₂ clusters in NiMoWS in accordance with electron microscopy. As a final step of the XAS data analysis, a multi-edge, multi-scattering fit procedure was applied to analyze the EXAFS of the sulfides at all metal edges simultaneously. The three references, MoS₂, WS₂, and Ni₃S₂ were fitted by using FEFF paths calculated from the crystallographic structure. The fit of the EXAFS and the corresponding Fourier transforms of the references are presented in Figure S12–S14 and Tables S3–S5. MoS₂ and WS₂ showed the expected trigonal-prismatic coordination environment with the maximum metal–sulfur and metal–metal coordination of six, respectively. Ni₃S₂ was difficult to fit, since the distances to the 4S and the 4Ni neighbors were very close. Moreover, the two distances for Ni–S neighbors at 2.26 and 2.27 Å could not be differentiated and were, therefore, fitted together resulting in an overall coordination number of 4.4. The most intense single scattering paths up to 4.1 Å were added to the analysis to obtain an appropriate fit.

Table 2–4 summarize the best-fit results for the k^3 weighted EXAFS data of the sulfided catalysts at the Mo K-edge, W L_{III}-edge, and Ni K-edge. For the sulfide NiMoS catalyst (Table 2), full Mo–S coordination environment was found at the Mo K-edge, and the bond distances match those corresponding to MoS₂ (Figure S15 and S16 show the experimental EXAFS data compared to the fit). The presence of Mo–O neighbors at short distances was not required during the fit procedure. The $N_{\text{Mo-Mo}}$ in NiMoS was 5.1, which is below the coordination number in the reference MoS₂ ($N_{\text{Mo-Mo}}=6$). This implies that, although the metal was in a trigonal-prismatic environment, not all atoms have full coordination environment (i.e., metal atoms at the edges of the slabs). The value for $N_{\text{Ni-S}}=4.5$ (Table 4) indicates that Ni is either tetrahedrally or pentagonally coordinated by sulfur, which fits to the observed pre-edge feature of the XANES (Supporting Information). The second contribution at $r_{\text{Ni-Ni}}=2.6$ Å with $N_{\text{Ni-Ni}}=1.2$, as well as the third contribution at $r_{\text{Ni-Ni}}=3.9$ Å with $N_{\text{Ni-Ni}}=4.4$ were smaller than those in Ni₃S₂. The metal–metal coordination numbers (Mo–Mo) and (Ni–Ni), smaller in NiMoS than in the references, reflect lower crystallinity (smaller size of the MoS₂ slabs and Ni sulfide particles and large disorder). Moreover, other Ni sulfide phases than Ni₃S₂ are probably present as well. Additionally, a Ni–Mo contribution was observed at 2.7 Å with the coordination number of 0.2, which indicates that Ni is indeed associated with MoS₂. The quality of the fit was improved by 6.5% after adding this contribution. The assumption of a Mo–Ni contribution at the Mo K-edge and the associated constraints improved the fit further by 2%.

Table 2. Best-fit results for k^3 weighted EXAFS data of the sulfided catalysts at the Mo K-edge.^[a]

Catalyst	Shell	r [Å]	N	σ^2 [Å ²]	E_0 [eV]
NiMoS $R=0.0013$	Mo-S	2.40 (0.01)	6.2 (0.2)	0.0025 (0.0002)	0.74 (0.67)
	Mo-Mo	3.17 (0.01)	5.1 (0.1)	0.0033 (0.0001)	
	Mo-Ni	2.68 (0.02)	0.3 (0.1)	0.0024 (0.0022)	
NiMoWS $R=0.0055$	Mo-S	2.40 (0.01)	5.2 (0.1)	0.0027 (0.0002)	1.52 (0.60)
	Mo-Mo	3.16 (0.01)	3.1 (0.1)	0.0043 (0.0010)	
	Mo-W	3.17 (0.01)	1.6 (0.2)	0.0042 (0.0004)	
	Mo-Ni	2.68 (0.03)	0.6 (0.1)	0.0093 (0.0029)	

[a] Abbreviations: r : distance, N : coordination number, σ^2 : Debye–Waller like factor, E_0 : inner potential; in parenthesis the absolute errors.

In NiWS, W–S and W–W contributions were found at the same distances as in the reference WS₂ structure. The experimental and fitted EXAFS and FT at the W and Ni edge, are shown in Figure S17 and S18, results of the fits are summarized in Table 3 and Table S5. The coordination numbers $N_{\text{W-S}}$ and $N_{\text{W-W}}$ were 4.5 and 3.1, respectively. Both are smaller than for

Table 3. Best-fit results for k^3 weighted EXAFS data of the sulfided catalysts at the W L_{III} -edge in k space.^[a]

Catalyst	Shell	r [Å]	N	σ^2 [Å ²]	E_0 [eV]
NiWS $R=0.0033$	W-S	2.40 (0.01)	4.5 (0.2)	0.0037 (0.0002)	7.36 (0.44)
	W-W	3.15 (0.01)	3.1 (0.4)	0.0045 (0.0005)	
	W-Ni	2.75 (0.05)	0.1 (0.1)	0.0033 (0.0030)	
NiMoWS $R=0.0055$	W-S	2.41 (0.01)	4.9 (0.2)	0.0044 (0.0006)	8.02 (1.23)
	W-W	3.17 (0.02)	2.1 (0.3)	0.0042 (0.0006)	
	W-Mo	3.17 (0.01)	2.0 (0.2)	0.0042 (0.0004)	
	W-Ni	2.82 (0.04)	0.6 (0.2)	0.0030 (0.0021)	

[a] Abbreviations: r : distance, N : coordination number, σ^2 : Debye–Waller like factor, E_0 : inner potential; in parenthesis the absolute errors.

Table 4. Best fit results for k^3 weighted EXAFS data of the sulfided catalysts at the Ni K-edge in k space.^[a]

Catalyst	Shell	r [Å]	N	σ^2 [Å ²]	E_0 [eV]
NiMoS $R=0.0013$	Ni-S	2.27 (0.02)	4.5 (0.5)	0.0075 (0.0010)	3.00 (2.66)
	Ni-Ni	2.60 (0.03)	1.2 (0.5)	0.0071 (0.0031)	
	Ni-Mo	2.68 (0.02)	0.2 (0.1)	0.0024 (0.0022)	
	Ni-Ni	3.88 (0.06)	4.4 (3.5)	0.0169 (0.0076)	
NiWS $R=0.0033$	Ni-S	2.26 (0.01)	4.4 (0.6)	0.0089 (0.0013)	2.35 (1.51)
	Ni-Ni	2.57 (0.02)	0.5 (0.2)	0.0052 (0.0020)	
	Ni-W	2.75 (0.05)	0.1 (0.1)	0.0033 (0.0030)	
	Ni-Ni	3.97 (0.08)	3.1 (2.7)	0.0239 (0.0119)	
NiMoWS $R=0.0055$	Ni-S	2.27 (0.03)	3.8 (0.7)	0.0076 (0.0034)	2.85 (4.75)
	Ni-Ni	2.59 (0.05)	0.7 (0.5)	0.0055 (0.0045)	
	Ni-Mo	2.68 (0.03)	0.3 (0.1)	0.0093 (0.0029)	
	Ni-W	2.82 (0.04)	0.2 (0.2)	0.0030 (0.0021)	

[a] Abbreviations: r : distance, N : coordination number, σ^2 : Debye–Waller like factor, E_0 : inner potential; in parenthesis the absolute errors.

the reference WS_2 , which indicates smaller particle size and distortion in the catalyst. The addition of a W-O contribution at around 2 Å resulted in the degradation of the fit quality. Thus, its presence was excluded. The distances and coordination numbers of the first Ni-S contribution match those of Ni_3S_2 (Table 4). The second and third Ni-Ni contributions appear at 2.57 Å ($N_{Ni-Ni}=0.5$) and at 3.97 Å ($N_{Ni-Ni}=3.1$), i.e., the coordination numbers are much smaller and a shift of the Ni-Ni contribution is observed compared to Ni_3S_2 and NiMoS. These observations also suggest smaller particle sizes of different Ni sulfide phases in NiWS. The fit was slightly improved by adding W-Ni and Ni-W contributions at 2.75 Å, which indicates that also in NiWS, Ni associates to the WS_2 slabs although probably to a minor extent compared to NiMoS.

The results of the EXAFS analysis and the corresponding FT of the trimetallic NiMoWS catalyst are summarized in Tables 2 to 4 and Figure S19, S20, and S21. The Mo-S and W-S coordination numbers were both around 5.0, lower than in NiMoS, but higher than in NiWS. This reflects an intermediate sulfidation (less complete sulfur coverage at the edges) state for the trimetallic catalyst. Furthermore, as predicted by the EXAFS of

the model clusters, Mo-W and W-Mo contributions were found at 3.16 Å and 3.17 Å. The quality of the overall EXAFS fit improved by 25 % by using the FEFF-paths of the model $Mo_{1-x}W_xS_2$ cluster with N (Mo-W) of 3 (Particles 3(f) and 4(f)) as a model to fit the experimental EXAFS. At the Mo K-edge, $N_{Mo-Mo}=3.1$ and $N_{Mo-W}=1.6$ were found, which leads to an average Mo-metal coordination number of 4.7 at around 3.2 Å. The average N_{Mo-Ni} in NiMoWS is 0.6, i.e., twice as high as in NiMoS. The coordination numbers at the W L_{III} -edge for NiMoWS were 2.0 for N_{W-Mo} , 2.1 for N_{W-W} and 0.6 for N_{W-Ni} . The latter coordination number was higher than in the bimetallic NiWS catalyst. The finding of higher Mo-Ni and W-Ni coordination numbers in NiMoWS than in NiMoS and NiWS is important, because it indicates better interaction of Ni on the sulfide slabs in the trimetallic than in the bimetallic sulfides. For this NiMoWS catalyst, N_{Mo-Mo} is higher than N_{W-W} whereas N_{Mo-W} is lower than N_{W-Mo} . These observations suggest that the content of Mo and W within a sulfide slab is similar to that of the bulk (slightly more Mo than W, Table 1). Thus, most of the sulfide slabs must be $Mo_{1-x}W_xS_2$ particles containing both metals in one layer. N_{Ni-S} of 3.8 at $r_{Ni-S}=2.27$ Å was found in NiMoWS, which is the lowest N_{Ni-S} value among all measured samples. $N_{Ni-Ni}=0.7$ at 2.59 Å lies between the values compared to the bimetallic catalysts. The Ni-Mo contribution was found at a distance of 2.68 Å, which is the same as in NiMoS. A slightly longer distance was found for the Ni-W contribution in NiMoWS compared to that in NiWS (both are longer than the Ni-Mo distance). These mixed Ni-Mo and Ni-W contributions have higher coordination numbers than in the bimetallic catalyst, especially for Ni-W. The observations confirm that the Mo(W)-Ni incorporation was higher in the trimetallic than in both bimetallic catalysts.

Catalytic activity

The kinetic data are compiled in the Supporting information. Figure 12 summarizes the dependence of *o*-propylaniline (OPA) and dibenzothiophene (DBT) conversion rates on temperature.

OPA is converted to propylbenzene (PB) via a C_{sp}^2 -N cleavage (direct denitrogenation route, DDN); and to propylcyclohexylamine (PCHA) via hydrogenation of the benzoic ring. This hydrogenation route (HYDN) continues with fast nitrogen removal to propylcyclohexene (PCHE) via Hoffman-elimination and hydrogenation to propylcyclohexane (PCH).^[38] The HDS of DBT follows two pathways, direct desulfurization (DDS) and hydrogenation (HYDS). The former pathway has biphenyl (BiPh) as only product, whereas HYDS leads to tetrahydrodibenzothiophene (H-DBT), which is further hydrogenated to phenylcyclohexane (PhCH) or biphenyl (BiCH) via dodecahydrodibenzothiophene (DH-DBT).^[39] The reaction networks for HDN and HDS are illustrated in Figures S22 and S23. All mentioned products were found for all three catalysts.

The rates normalized to metal content were identical for both HDN and HDS with the HDN rates being 4–5 times higher than rates of HDS (Figure 12). The nearly identical energy of activation for related reactions suggests that the differences are caused by differences in the concentrations of active sites.

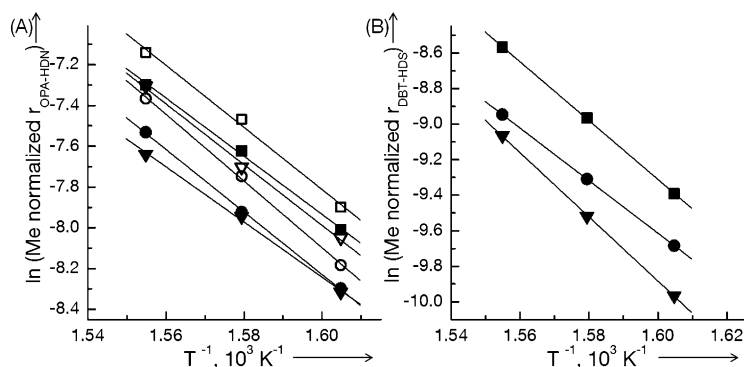


Figure 12. Hydrotreating activity normalized per metal content in function of temperature for the determination of the apparent activation energy for the HDN of OPA (A) and HDS of DBT (B) of NiMoS (\blacktriangledown), NiMoWS (\blacksquare) and NiWS (\bullet). The HDN rates in the absence of DBT are as well shown (open symbols \square \triangleright \circ).

NiMoWS exhibited the highest conversion rates followed by the bimetallic NiWS and NiMoS, which had similar HDN rates. The presence of DBT decreased the HDN rates, especially on NiMoS, without showing impact on the selectivity (Figure 13 for NiMoWS and in the Supporting Information for the bimetallic catalysts). The HDN rates in absence of DBT were higher for NiMoS than for NiWS, whereas NiWS had the higher HDN rates in the presence of DBT. In this regard, the HYDN route was faster than DDN by one order of magnitude. In contrast, the HYDS route was slower than DDS also by one order of magnitude. The marked preference for DDS is illustrated by the selectivity towards BiPh, Figure 13(B). The apparent activation energies (E_a) for the DDN route were larger than those of the HYDN route. For instance, 191–230 kJ mol^{-1} (DDN) and 119–129 kJ mol^{-1} (HYDN), in the absence of DBT (Table S6). In general, the presence of DBT decreased the E_a values of both routes slightly, which is hypothesized to indicate that the adsorption of OPA becomes stronger in the presence of DBT (more negative adsorption enthalpies would decrease the apparent activation energies). The apparent activation energies for the DDS route of HDS were 137 kJ mol^{-1} for NiMoS, 139 kJ mol^{-1} for NiMoWS and 148 kJ mol^{-1} for NiWS. The E_a

values of the HYDS route increased in the order NiWS < NiMoWS < NiMoS (the very low yields of the products of this route hinder quantitative discussion).

Structure activity correlations

Control experiment have shown that species of Ni sulfides are relatively unreactive for HDN and HDS, compared to Mo(W)S₂ phases. Therefore, in the following only Mo(W)S₂ species are discussed as catalytically active. All estimated rates in the HDS and HDN reaction of the trimetallic NiMoWS sulfide catalyst were higher than those of bimetallic catalysts. The properties determining the activity of sulfide catalysts are the dispersion of the active phase and type of active sites, as both together control the concentration, availability, and its intrinsic activity. Especially,

Lewis acidic sulfur vacancies (CUS) acting as adsorption sites and Brønsted acidic -SH groups providing hydrogen are essential for hydrotreating.^[4,40] The -SH groups are not only needed for the hydrogenation steps, but also to provide hydrogen during the cleavage of the carbon-heteroatom bonds and could act as weak adsorption site.^[4,38] The intrinsic activity is influenced by the nature of the active phase (WS₂ or MoS₂), the sulfidation degree, and the concentration of Ni. The dispersion is determined by the sulfide morphology and particle size. Therefore, the higher activity of NiMoWS suggests a higher concentration and/or availability of CUS and -SH groups compared to the bimetallic sulfides.

The trimetallic sulfide has intralayer mixed Mo_{1-x}W_xS₂ slabs and an average metal-sulfur coordination number of 5, whereas the N_{W-5} was only 4.5 for WS₂ in NiWS. For NiMoS the N_{Mo-5} of 6 suggests fully coordinated Mo atoms in MoS₂. An average metal-sulfur coordination number lower than 6 for the W-containing sulfides suggest the presence of CUS (reduced edges) or of distorted sulfide structures. The metal-sulfur coordination is especially interesting to analyze for WS₂, since the sulfidation of W oxides is slower than that of Mo oxides (W-O bond strength of 7.0 eV compared to 5.8 eV of Mo-O).^[41] In turn, the activity of Ni-WS₂ has been correlated to its sulfidation degree.^[42,43] The results demonstrate, however, that the contribution of oxide species is minor for both W containing catalysts as deduced from LCF and EXAFS, both pointing to a nearly complete sulfidation. Thus, the relatively low N_{W-5} values are attributed to the bent and less aligned morphology.

Differences in morphology and particle size were observed between the three unsupported catalysts. The highest stacking degree was observed for NiMoS, the largest sulfide slabs for NiMoWS, and the most disordered slabs for NiWS. Thus, we conclude that the low N_{W-5} value in NiWS is caused by distortion and bending of WS₂ slabs, which leads to variations in bond length and angles. Therefore, in the EXAFS not all sulfur neighbors were visible at the normal distance, leading to an underestimation of the sulfur coordination number.^[33] The same is concluded to

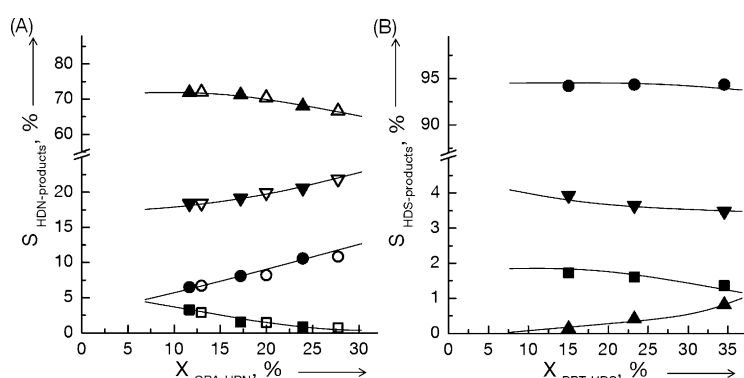


Figure 13. Selectivities along with conversion over NiMoWS for (A) OPA HDN and (B) DBT HDS. The products in (A) are PCHE (\blacktriangle), PCH (\blacktriangledown), PB (\bullet), and PCHA (\blacksquare). The HDN selectivities are presented in the presence of DBT (black symbols \blacktriangle \blacktriangledown \bullet \blacksquare) and in the absence of DBT (open symbols \triangle \triangleright \circ \square). The products in (B) are BiPh (\bullet), BiCH (\blacktriangledown), H-DBT (\blacksquare), and PhCH (\blacktriangle).

occur in NiMoWS as suggested by the strong sulfide slab bending. Such exposed sulfur atoms in a distorted environment are more labile and, hence, easier to remove to create CUS, which is connected to a formal reduction to W or Mo. Note that for the pure MoS₂ and WS₂ phases, the metal–S bond strength is 2.6 eV, and 2.9 eV, respectively,^[44] suggesting that only small differences in the reduction degree of MoS₂ and WS₂ are probable. However, the substitution of W by Ni might be more effective for WS₂ than for MoS₂, leading to higher CUS concentration than for promoted MoS₂.^[32] In contrast, the well-ordered highly stacked slabs, i.e., high crystallinity, as observed for NiMoS influences the active site concentration negatively and, in turn, lowers the activity. Note in passing that increasing particle size and stacking degree increase are among the causes of deactivation. Thus, we conclude that both W containing catalysts have a higher CUS concentration, in line with their higher activity compared to NiMoS.

CUS and -SH groups are located at the perimeter, i.e., at exposed edges of the Mo and W sulfide slabs. Considering hexagonal geometry, the number of Mo and W atoms at the edges of a sulfide particle derived from the average slab lengths, is 185 atoms for NiMoWS, 134 atoms for NiWS and 91 atoms for NiMoS per slab.^[45] The trend for the edge atoms of the catalysts matches the found activity trend in HDS, i.e., the larger the slab the higher the HDS activity. However, the average fraction of Mo and W at the sulfide edge in relation to the total number of Mo and W atoms per sulfide slab^[45] results in very low values for large particles such as in NiMoWS ($f_{\text{Mo,W}} = 0.06$) and NiWS ($f_{\text{W}} = 0.08$). This fraction is used as a measure for the dispersion of supported sulfide systems, low dispersion accounts for low hydrotreating activity.^[39,46] This apparent contradiction is resolved by considering that the slabs of the catalysts are neither rigid nor straight. We speculate that the distortion of large sulfide slabs strongly increases the active site concentration.

Following the hypothesis that small, poorly crystalline sulfide particles are required for high catalytic activity, NiWS would be expected to be more active than NiMoWS based on its shorter sulfide slabs and the lower metal–sulfur coordination numbers. The question also arises as to why NiMoWS is more active than the strongly disordered NiWS, whereas at the same time the HDN rate on NiMoS was comparable to the HDN rate of NiWS. As discussed below the answer is related to the nature of the reactive perimeter and the way Ni influences it.

Hydrogenation has been found to scale with the concentration of -SH groups, which are created by dissociative adsorption of H₂S and H₂ at CUS. The incorporation of Ni in MoS₂/Al₂O₃ increased the concentration of -SH groups,^[40] leading in turn to a correlation of the hydrogenation rates to the Ni concentration.^[38,47] The incorporation of Ni occurs on the edges of mixed sulfide phases, i.e., Mo(W)S₂ slabs.^[48] All three materials contained large concentrations of Ni and Ni-promoted MoS₂ and WS₂ cations were identified by probe molecules (here not presented). In NiMoWS, the highest coordination numbers for Mo–Ni (Ni–Mo) and W–Ni (Ni–W) were observed as well as $N_{\text{Ni–S}}$ of 3.8 (the lowest value in the series). The intermetallic coordination numbers in the bimetallic catalysts are low compared

to NiMoWS with $N_{\text{Mo–Ni}}$ and $N_{\text{W–Ni}}$ of 0.3 and 0.1 in NiMoS and NiWS, respectively. Therefore, the interaction between the intralayer mixed Mo_{1–x}W_xS₂ phase in NiMoWS and the promoter Ni is concluded to be more effective than with the pure MoS₂ and WS₂ phase.

The formation of promoted sulfide phases has been demonstrated for Ni–W and bulk sulfides^[13,32,34,49] and is indicated by the significant mixed metallic coordination numbers (Mo–Ni or W–Ni). It is concluded that the concentration of Ni-promoted sulfide CUS was higher for NiMoWS than for NiMoS, which translates to an increased -SH concentration. The interactions of Ni with WS₂ in NiWS are in contrast very weak.

It is hypothesized that the faster sulfidation rates for Mo species than for W increases the probability of incorporation of Ni. In addition to the Ni promoting species, the formation of a variety of Ni sulfide species is observed. The relatively low $N_{\text{Ni–Ni}}$ values deduced from EXAFS compared to the reference Ni₃S₂ are attributed to the existence of several Ni–Ni distances and $N_{\text{Ni–Ni}}$ values broadening the corresponding EXAFS. In line with this hypothesis, different Ni sulfide phases were observed by XRD and electron microscopy. Note, that in NiMoS, $N_{\text{Ni–Ni}}$ at 2.6 Å is 1.2, whereas in NiWS and NiMoWS, $N_{\text{Ni–Ni}}$ at around the same distance is 0.5 and 0.7, respectively. This indicates that the NiS_x particles are, in average, smaller when interacting with WS₂ or Mo_{1–x}W_xS₂.^[32]

Thus, the performance of unsupported NiMoS is dominated by the Ni promoted MoS₂ phase. Ni- and Mo-associated CUS are present, which act as adsorption and reaction sites for OPA, DBT, and H₂. However, the overall concentration of active sites is lower compared to NiMoWS due to the morphology of NiMoS. Therefore, the reactants compete for fewer Ni-promoted sites, which is in line with the very low conversion rate for the HYDS route of DBT and the decrease of the conversion rate for the HYDN route in the presence of DBT. The DDN rates were hardly affected by DBT because the active sites for DDN are Mo associated sites instead of Ni-CUS.^[38]

The morphology of WS₂ appears to be better suited to stabilize a high active site concentration. The fraction of Ni promoted WS₂ is relatively low compared to NiMoS, however, the high hydrogenation rates of DBT and OPA in presence of DBT (Figures S25–S26 and Table S6) might be due to higher intrinsic activity of the Ni-promoted W sites. This is consistent with the reported higher hydrogenation rates for Ni–W sulfides compared to Ni–Mo,^[50] being more active for, e.g., HDS of substituted dibenzothiophenes (for which hydrogenation is critical in the reaction pathway).^[51,52] These sites are less active to convert OPA via the HYDN route in the absence of DBT compared to NiMoS. However, in the presence of DBT the HYDN rates decrease at most by 18%, whereas in NiMoS a decrease of up to 43% was observed. This suggests that the W associated sites are less affected by the presence of DBT.

The unsupported trimetallic NiMoWS catalyst exhibit a mixture of the sites and structural features found in NiMoS and NiWS. This is also indicated by the activation energies of the catalytic routes being in between the values observed on NiMoS and NiWS. Moreover, this mixture results in a higher density of active sites. It is concluded that the intralayer mix-

ture (Mo and W present in the same slab) is synergistic for the hydrotreating activity, stabilizing a concentration of Ni-promoted sites and a high concentration of -SH groups. The intralayer $\text{Mo}_{1-x}\text{W}_x\text{S}_2$ phase enabled the growth of long slabs with a moderate stacking degree and a distortion providing a high edge area and, therefore, a higher CUS concentration than in NiWS. The higher concentration of Ni in the $\text{Mo}_{1-x}\text{W}_x\text{S}_2$ mixed phase compared to NiMoS is concluded to lead in turn to a higher -SH group concentration.

Conclusions

All three mixed sulfide phases, i.e., NiMoS, NiWS, and NiMoWS offer interesting possibilities for hydrogenation, hydrodesulfurization as well as hydrodenitrogenation. The characterization suggests that all catalysts consist of mixtures of Ni containing Mo(W)S₂ and Ni sulfides (Ni₉S₈, Ni₃S₂, and Ni₃S₄). The (Ni)Mo(W)S₂ phase is formed by stacks of 4–6 sulfide slabs with some degree of bending and mismatch between the layers. Stacks of the sulfide particles agglomerate in random directions forming spheres with sizes in the submicron range on a mesoscopic level. The Ni sulfides show in contrast a broad distribution of particle sizes ranging from few microns, on which the Mo(W)S₂ agglomerates deposit, to small particles completely covered by the Mo(W)S₂ domains.

Microscopy images with atomic resolution showed metal (Mo or W) rich stacks of atoms with remarkable differences in Z-contrast in NiMoWS, which suggested the formation of intralayer $\text{Mo}_{1-x}\text{W}_x\text{S}_2$ particles (Mo and W in the same sulfide slabs), as well as the preference of alignment of homotopic cations in the projection direction of the STEM measurements. To confirm this hypothesis series of model clusters were constructed and the corresponding EXAFS were calculated. Models with interlayer $\text{Mo}_{1-x}\text{W}_x\text{S}_2$ particles (slabs of MoS₂ and WS₂ stacked in different sequences) and intralayer $\text{Mo}_{1-x}\text{W}_x\text{S}_2$ particles were considered. The analysis of the theoretical EXAFS showed that the presence of mixed Mo and W in different slabs did not influence the EXAFS and Fourier transforms at the Mo (K-edge). In contrast, the presence of W in close vicinity of Mo within a sulfide slab decreased the metal–metal (Mo–W or W–Mo) backscattering. This was caused by destructive interference between the Mo–W and Mo–Mo scattering pairs with opposite phases. The same effect was observed in the EXAFS and Fourier transforms of the NiMoWS catalyst, which suggested the formation of sulfides slabs with Mo and W.

The EXAFS fittings of bimetallic and the trimetallic sulfides confirm the presence of MoS₂, WS₂, in NiMoS and NiWS, respectively showing smaller coherent domains than the reference materials. The EXAFS fitting of NiMoWS confirms the presence of intralayer $\text{Mo}_{1-x}\text{W}_x\text{S}_2$. The presence of Ni–Mo (Mo–Ni), and Ni–W (W–Ni) paths in all materials suggests that Ni is effectively interacting with MoS₂, WS₂, or $\text{Mo}_{1-x}\text{W}_x\text{S}_2$, allowing us to conclude that mixed Ni–Mo(W) sulfide phases were present in all catalysts. The values of the coordination numbers suggest that the most pronounced Mo(W)–Ni interaction occurs in the trimetallic NiMoWS. The nature of the promoting Ni species, i.e., single atoms (like in a classic Ni–Mo–S model^{[53])} or

clusters^[47] remains unresolved as evidence of Ni atoms at the edges of Mo(W)S₂ slabs and/or defined Mo(W)S₂–NiS_x phases^[54] were not observed by microscopy. The small Ni–Ni coordination numbers suggest that a substantial fraction of NiS_x consists of very small clusters or atomically dispersed Ni.

The catalytic properties (hydrodesulfurization of dibenzothiophene and hydrodenitrogenation of *o*-propylaniline) were governed by the concentration of accessible cations and the concentration of -SH groups. The trimetallic catalyst had the highest concentration of active sites leading to the highest HDN and HDS rates. The trimetallic sulfide was, thus, concluded to have the largest specific perimeter. We conclude that the simultaneous presence of Mo and W in the same slab in NiMoWS retards the growth and favors nucleation of Ni promoting species, allowing so the largest fraction of Ni to be incorporated. The additional slow growth in *z* direction leads to a maximizing of the active sites at the perimeter of the particles.

Acknowledgements

This work was supported by the Chevron Energy Technology Company. The authors would like to specially thank Dr. Alexander Kuperman, and Dr. Jinyi Han for fruitful discussions. We thank Prof. Roel Prins for the critical review of the results and Prof. Matthias Bauer and Prof. Moniek Tromp for their assistance throughout the whole presented work. The authors acknowledge the light source facility DORIS III at DESY (member of the Helmholtz Association, Germany) and ESRF (Grenoble, France) for the provision of beam time as well as the HASYLAB staff at DESY (beamline X1) and the DUBBLE staff at ESRF. We are also grateful to Dr. Marianne Hanzlik for TEM measurements, Dipl.-Min. Katia Rodewald for HR-SEM measurements (Institute of Silicon Chemistry, TU Munich) and Dipl.-Ing. Xaver Hecht for technical support. Further, Robert Colby and Bernd C. Kabius from PNNL are acknowledged for the SHIM measurements.

Keywords: electron microscopy · hydrodenitrogenation · hydrodesulfurization · hydrotreating · multimetallic sulfides · X-ray absorption spectroscopy

- [1] W. Bensch in *Comprehensive Inorganic Chemistry II, 2nd ed.* (Eds.: J. Reedijk, K. Poeppelmeier), Elsevier, Amsterdam, **2013**, pp. 287–321.
- [2] R. Prins, *Adv. Catal.* **2001**, *46*, 399–464.
- [3] R. R. Chianelli, G. Berhault, B. Torres, *Catal. Today* **2009**, *147*, 275–286.
- [4] O. Y. Gutiérrez, A. Hrabar, J. Hein, Y. Yu, J. Han, J. A. Lercher, *J. Catal.* **2012**, *295*, 155–168.
- [5] P. M. Mortensen, J. D. Grunwaldt, P. A. Jensen, K. G. Knudsen, A. D. Jensen, *Appl. Catal. A* **2011**, *407*, 1–19.
- [6] U. Maitra, U. Gupta, M. De, R. Datta, A. Govindaraj, C. N. R. Rao, *Angew. Chem. Int. Ed.* **2013**, *52*, 13057–13061; *Angew. Chem.* **2013**, *125*, 13295–13299.
- [7] J. P. Wilcoxon, T. R. Thurston, J. E. Martin, *Nanostruct. Mater.* **1999**, *12*, 993–997.
- [8] T. F. Jaramillo, K. P. Jørgensen, J. Bonde, J. H. Nielsen, S. Horch, I. Chorkendorff, *Science* **2007**, *317*, 100–102.
- [9] J. N. Coleman, M. Lotya, A. O'Neill, S. D. Bergin, P. J. King, U. Khan, K. Young, A. Gaucher, S. De, R. J. Smith, I. V. Shvets, S. K. Arora, G. Stanton, H. Y. Kim, K. Lee, G. T. Kim, G. S. Duesberg, T. Hallam, J. J. Boland, J. J. Wang, J. F. Donegan, J. C. Grunlan, G. Moriarty, A. Shmeliov, R. J. Nich-

- olls, J. M. Perkins, E. M. Grieveson, K. Theuwissen, D. W. McComb, P. D. Nellist, V. Nicolosi, *Science* **2011**, *331*, 568–571.
- [10] B. T. Yonemoto, G. S. Hutchings, F. Jiao, *J. Am. Chem. Soc.* **2014**, *136*, 8895–8898.
- [11] D. O. Dumcenco, H. Kobayashi, Z. Liu, Y.-S. Huang, K. Suenaga, *Nat. Commun.* **2013**, *4*, 1351.
- [12] Y. Zhu, Q. M. Ramasse, M. Brorson, P. G. Moses, L. P. Hansen, C. F. Kisielowski, S. Helveg, *Angew. Chem. Int. Ed.* **2014**, *53*, 10723–10727; *Angew. Chem.* **2014**, *126*, 10899–10903.
- [13] S. D. Kelly, N. Yang, G. E. Mickelson, N. Greenlay, E. Karapetrova, W. Sinker, S. R. Bare, *J. Catal.* **2009**, *263*, 16–33.
- [14] J. Hein, A. Hrabar, A. Jentys, O. Y. Gutiérrez, J. A. Lercher, *ChemCatChem* **2014**, *6*, 485–499.
- [15] S. P. A. Louwers, R. Prins, *J. Catal.* **1992**, *133*, 94–111.
- [16] S. Eijsbouts, S. W. Mayo, K. Fujita, *Appl. Catal. A* **2007**, *322*, 58–66.
- [17] J. Bocarando, R. Huirache-Acuña, W. Bensch, Z. D. Huang, V. Petranovskii, S. Fuentes, G. Alonso-Núñez, *Appl. Catal. A* **2009**, *363*, 45–51.
- [18] S. Srivastava, D. Palit, *Solid State Ionics* **2005**, *176*, 513–521.
- [19] D. O. Dumcenco, Y.-C. Su, Y.-P. Wang, K.-Y. Chen, Y.-S. Huang, C.-H. Ho, K.-K. Tiong, *Solid State Phenom.* **2011**, *170*, 55–59.
- [20] T. Maesen, A. E. Kuperman, US 2009/007883, United States, **2008**.
- [21] A. Belsky, M. Hellenbrandt, V. L. Karen, P. Luksch, *Acta Crystallogr. Sect. B* **2002**, *58*, 364–369.
- [22] J. J. Rehr, J. J. Kas, F. D. Vila, M. P. Prange, K. Jorissen, *Phys. Chem. Chem. Phys.* **2010**, *12*, 5503–5513.
- [23] K. V. Klementiev, VIPERfreeware, K. V. Klementev, *J. Phys. D* **2001**, *34*, 209.
- [24] B. Ravel, M. Newville, *J. Synchrotron Radiat.* **2005**, *12*, 537–541.
- [25] S. I. Zabinsky, J. J. Rehr, A. Ankudinov, R. C. Albers, M. J. Eller, *Phys. Rev. B* **1995**, *52*, 2995–3009.
- [26] D. Yang, R. F. Frindt, *Mol. Cryst. Liq. Cryst. A* **1994**, *244*, 355–360.
- [27] J. Moser, F. Lévy, *Thin Solid Films* **1994**, *240*, 56–59.
- [28] C. Lee, H. Yan, L. E. Brus, T. F. Heinz, J. Hone, S. Ryu, *ACS Nano* **2010**, *4*, 2695–2700.
- [29] J. W. Chung, A. Adib, Z. R. Dai, K. Adib, F. S. Ohuchi, *Thin Solid Films* **1998**, *335*, 106–111.
- [30] L. Wang, Y. Zhang, Y. Zhang, Z. Jiang, C. Li, *Chem. Eur. J.* **2009**, *15*, 12571–12575.
- [31] L. P. Hansen, Q. M. Ramasse, C. Kisielowski, M. Brorson, E. Johnson, H. Topsøe, S. Helveg, *Angew. Chem. Int. Ed.* **2011**, *50*, 10153–10156; *Angew. Chem.* **2011**, *123*, 10335–10338.
- [32] E. J. M. Hensen, Y. van der Meer, J. A. R. van Veen, J. W. Niemantsverdriet, *Appl. Catal. A* **2007**, *322*, 16–32.
- [33] T. Shido, R. Prins, *J. Phys. Chem. B* **1998**, *102*, 8426–8435.
- [34] C. Thomazeau, C. Geantet, M. Lacroix, M. Danot, V. Harle, *Oil Gas Sci. Technol.* **2005**, *60*, 781–790.
- [35] C. Thomazeau, C. Geantet, M. Lacroix, V. Harlé, S. Benazeth, C. Marhic, M. Danot, *J. Solid State Chem.* **2001**, *160*, 147–155.
- [36] M. Bauer, H. Bertagnolli in *Methods in Physical Chemistry* (Eds.: P. R. Schäfer, P. P. C. Schmid), Wiley-VCH, **2012**, pp. 231–269.
- [37] B. K. Teo, P. A. Lee, *J. Am. Chem. Soc.* **1979**, *101*, 2815–2832.
- [38] A. Hrabar, J. Hein, O. Y. Gutiérrez, J. A. Lercher, *J. Catal.* **2011**, *281*, 325–338.
- [39] O. Y. Gutiérrez, S. Singh, E. Schachtl, J. Kim, E. Kondratieva, J. Hein, J. A. Lercher, *ACS Catal.* **2014**, *4*, 1487–1499.
- [40] E. Schachtl, E. Kondratieva, O. Y. Gutiérrez Tinoco, J. A. Lercher, *J. Phys. Chem. Lett.* **2015**, *6*, 2929–2932.
- [41] *CRC Handbook of Chemistry and Physics, 90th ed.*, Internet Version, CRC Press, Boca Raton, FL, **2010**.
- [42] H. R. Reinhoudt, R. Troost, A. D. van Langeveld, J. A. R. van Veen, S. T. Sie, J. A. Moulijn, *J. Catal.* **2001**, *203*, 509–515.
- [43] M. J. Vissenberg, Y. van der Meer, E. J. M. Hensen, V. H. J. de Beer, A. M. van der Kraan, R. A. van Santen, J. A. R. van Veen, *J. Catal.* **2001**, *198*, 151–163.
- [44] H. Toulhoat, P. Raybaud, S. Kasztelan, G. Kresse, J. Hafner, *Catal. Today* **1999**, *50*, 629–636.
- [45] S. Kasztelan, H. Toulhoat, J. Grimblot, J. P. Bonnelle, *Appl. Catal.* **1984**, *13*, 127–159.
- [46] E. J. M. Hensen, P. J. Kooyman, Y. van der Meer, A. M. van der Kraan, V. H. J. de Beer, J. A. R. van Veen, R. A. van Santen, *J. Catal.* **2001**, *199*, 224–235.
- [47] E. Schachtl, E. Kondratieva, L. Zhong, J. Hein, O. Y. Gutiérrez, A. Jentys, J. A. Lercher, *ChemCatChem* **2015**, DOI: 10.1002/cctc.201500706.
- [48] H. Topsøe, B. S. Clausen, *Catal. Rev.* **1984**, *26*, 395–420.
- [49] A. Olivas, D. H. Galván, G. Alonso, S. Fuentes, *Appl. Catal. A* **2009**, *352*, 10–16.
- [50] J. A. R. van Veen in *Zeolites for Cleaner Technologies* (Eds.: M. Guisnet, J.-P. Gilson), Imperial College Press, **2002**, pp. 131–152.
- [51] W. R. A. M. Robinson, J. A. R. v. Veen, V. H. J. d. Beer, R. A. v. Santen, *Fuel Energy Abstr.* **2000**, *41*, 79–80.
- [52] T. Kabe, Y. Aoyama, D. Wang, A. Ishihara, W. Qian, M. Hosoya, Q. Zhang, *Appl. Catal. A* **2001**, *209*, 237–247.
- [53] M. W. J. Craje, S. P. A. Louwers, V. H. J. De Beer, R. Prins, A. M. Van der Kraan, *J. Phys. Chem.* **1992**, *96*, 5445–5452.
- [54] M. Ramos, G. Berhault, D. A. Ferrer, B. Torres, R. R. Chianelli, *Catal. Sci. Technol.* **2012**, *2*, 164–178.

Received: July 17, 2015

Published online on September 25, 2015